Available online at www.sciencedirect.com
ScienceDirect
Trans. Nonferrous Met. Soc. China 34(2024) 812−832
Transactions of Nonferrous Metals Society of China
www.tnmsc.cn

Microstructure evolution and deformation behaviors of AZ31 Mg alloy sheets processed by repeated bending−flattening deformation with different die angles

Min-hao LI[1], Li-wei LU[1,2,3], Yu-tian FAN[3], Min MA[3], Zhi-qiang WU[3], Tao ZHOU[4], Fu-gang QI[5], Hua ZHANG[6]

1. School of Mechanical Engineering, Hunan University of Science and Technology, Xiangtan 411201, China;
2. Hunan Provincial Key laboratory of High Efficiency and Precision Machining of Difficult-to-cut Material, Hunan University of Science and Technology, Xiangtan 411201, China;
3. School of Materials Science and Engineering, Hunan University of Science and Technology, Xiangtan 411201, China;
4. College of Materials Science and Engineering, Chongqing University of Technology, Chongqing 400054, China;
5. School of Materials Science and Engineering, Xiangtan University, Xiangtan 411105, China;
6. Institute for Advanced Studies in Precision Materials, Yantai University, Yantai 264005, China

Received 15 August 2022; accepted 26 June 2023

Abstract: AZ31 magnesium alloy sheets were fabricated by repeated bending−flattening deformation (RBFD) using dies of various angles. The microstructure evolution and deformation behaviors of the AZ31 Mg alloy during RBFD were investigated by FEM, OM, EBSD and hardness tester. The results suggest that the 150°/150° die exhibits the superior performance across all three groups. With an increase in passes, the effective strain of the alloy is significantly improved due to the positive impact of shear and bending. After four passes, the average grain size can be significantly refined to 1.7 μm, and a weaker basal texture can be obtained compared to the initial one due to non-basal slips, dynamic recrystallization (DRX), and twinning. Particularly, the pyramidal ⟨*c*+*a*⟩ slip promotes DRX and twinning. The hardness of the alloy reaches HV 77 as a result of the comprehensive effect of microstructure and texture generated by slip, twinning and DRX competition.

Key words: AZ31 Mg alloy sheet; microstructure evolution; deformation behavior; repeated bending−flattening process; die angle

1 Introduction

Magnesium alloy is considered to be the “green engineering material of the 21st century” and is also recognized as one of the most significant lightweight metals. Mg alloys are widely used in 3C electronic devices, aircraft, military industry and other fields [1], due to their advantages such as low density, high specific strength and stiffness, dimensional stability and ease of recycling [2]. However, the utilization of Mg alloys is limited by their low strength and plasticity at room temperature, which can be attributed to their special hexagonal close-packed (HCP) crystal structure [3,4]. Thus, extensive research has been carried out by scholars all over the world to enhance the mechanical properties of Mg alloys [5,6]. Grain refinement is an effective method for enhancing the strength and plasticity of Mg alloys, as well as strengthening the grain boundary co-deformation ability in HCP structure alloys. WANG et al [7] have shown that the strength and plasticity of Mg alloy sheets depend on the direction of tensile and micro-

Corresponding author: Li-wei LU, Tel: +86-17773201878, E-mail: cqullw@163.com
DOI: 10.1016/S1003-6326(23)66436-2

structure characteristics. KANG et al [8] have successfully refined the grain size of a new type of Mg alloy sheet from 80 to 22.4 and 15.9 μm through pre-aging and high-temperature extrusion deformation, resulting in impressive yield tensile strength (YTS), ultimate tensile strength (UTS) and elongation to failure (FE) of 217 MPa, 346 MPa, and 13.6%, respectively. SHENG et al [9] also refined the grains of Mg alloy to be less than 25 μm, resulting in a significant improvement in mechanical properties for all parts, including the fracture position. This reveals that grain refinement is beneficial to enhancing mechanical properties.

Severe plastic deformation (SPD) is an excellent method to achieve grain refinement, which involves techniques such as high pressure and torsion (HPT), equal channel angular pressing (ECAP), accumulative roll bonding (ARB), and repetitive corrugation and straightening (RCS). WU et al [10] have carried out the repeated plastic working process to refine the grain size of AZ31 Mg alloy to 500 nm, resulting in the maximum YTS and UTS of 330.5 and 362.3 MPa at room temperature, respectively, which were due to the enhanced and uniformly distribution of *I*-phase particles. KIM et al [11] investigated the micro-structure, texture, and mechanical properties of AZ31 Mg alloy after the ECAP. They found that the average grain size of the Mg alloy was refined to be 2.2 μm, resulting in notable enhancements in its mechanical performance. LUO et al [12] reported that refined grains inside the stress concentration areas are less prone to plastic deformation, requiring a larger external force to activate the plastic deformation of the adjacent grains. This leads to an increase in both YTS and elongation, especially uniform failure elongation (UFE), and strengthening basal plane texture is more likely to result from activating basal slip systems. However, the production of Mg alloys through simple SPD techniques is also subjected to various constraints such as extrusion process parameters (size, speed, temperature, load) changes in thickness and other factors. Excitingly, a similar experimental process was carried out by WANG et al [13,14], and found that as the compound deformation factor increases, the grain size decreases, the volume fraction of dynamic recrystallization (DRX) increases and the DRX gradually covers the original twins, and uniformly distributed and fine equiaxed grains are obtained, effectively improving the mechanical properties of magnesium alloy.

Therefore, the repeated bending−flattening deformation (RBFD) process was created as a new SPD processing technology for Mg alloy sheets, which completely takes the advantages of bending and flattening into account. Our method also has the following advantages: subsequent development is not limited by die and workpiece sizes; deformation is gentle, minimizing crack formation with upper and lower compressive stresses as the main force; operation is simple.

2 Experimental

Figure 1 shows bending die schematic and 3D flow chart of the RBFD process in a single pass. As shown in Fig. 1(a), the experimental groups were divided into three groups based on different angles of bending dies, with top angles (α/β) of 120°/120°, 120°/150°, and 150°/150° designated as Groups A, B, and C, respectively. In Fig. 1(b), each pass can

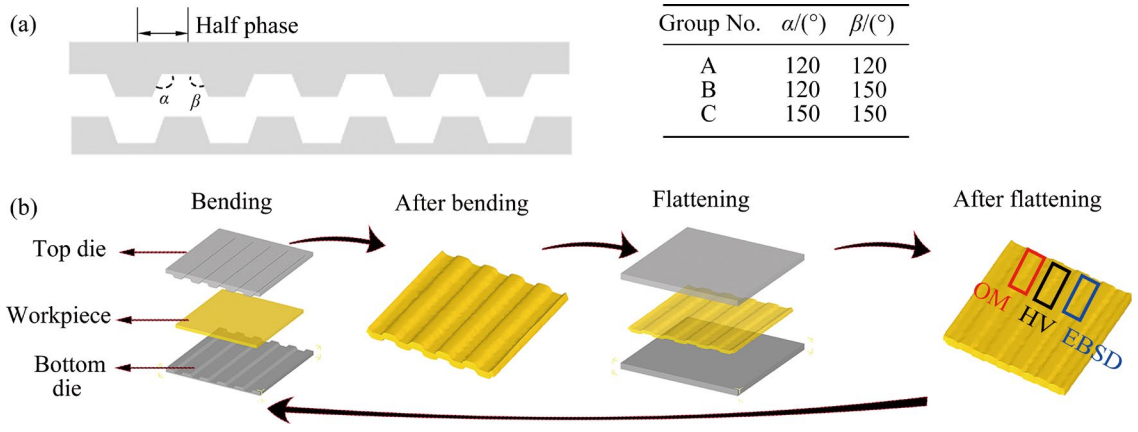

Group No.	α/(°)	β/(°)
A	120	120
B	120	150
C	150	150

Fig. 1 Bending die schematic (a) and 3D flow chart (b) of RBFD process with different dies in single pass

be divided into two half passes, namely the first and second half passes. The first half pass involves placing the workpiece between the bending dies, with the bottom die fixed and the top die moving from top to bottom in order to achieve the desired bend. During the second half pass, the workpiece is placed in a flattening die to restore its original flatness. The deformation process for each group involves a total of four passes, with the approach in Fig. 1(b) being repeated four times as previously introduced to complete the process.

The dies and workpiece were modeled in Solidworks software, and then imported into DEFORM 3D software for further analysis. The workpiece material was AZ31 Mg alloy. The deformation temperature was set to be 300 °C, the mesh division was set to be 60000 elements, and shear friction was used with a coefficient of friction of 0.3. The thermal conductivity was 5 W/(mm·°C), and the step size was 0.1 mm/step. After the simulation of the bending process, the flattening die was imported, and its position relative to the workpiece was adjusted to simulate the flattening process under the same working conditions. The simulation was repeated four times. To make the deformation strain more uniform, the initial position of the top die was used as the reference system, and the top die was moved by "half phase" distance in the 2nd pass and the 4th pass, as shown in Fig. 1(a). After simulation, effective strain clouds and flow rate vector diagrams of the 2nd pass and the 4th pass were derived, and the appropriate color bar range was set for preferable comparison.

As shown in Fig. 1, the sheets and dies were then heated to 300 °C, and held at this temperature for 10 min. Then, they were placed on the punching machine for pressing, and the RBFD experiment was completed after four deformation passes. As shown in the red box in Fig. 1(b), the processed sheets were cut into slices. Each slice was 6 mm in length and 8 mm in width, and four slices were cut from each sheet. Afterwards, the slices were polished with sandpaper of varying grit sizes (800#, 1000#, and 1200#), followed by surface diamond polishing using a polishing machine. Finally, they were etched for 40 s in an etching solution consisting of oxalic acid (1 g), nitric acid (1 mL), and water (98 mL). The microstructure was observed using a metallurgical microscope (OM), and the homogeneity of the microstructure was quantified and analyzed from the edge to the center. Following OM analysis, as shown in the blue box in Fig. 1(b), these sheets were cut into slices with dimensions of 8 mm in length and 6 mm in width. The inner slices of three groups were investigated by EBSD using a Nordlys Nano equipped with HKL Channel 5 software, operating at 20 kV and a scan step size of 0.75. Misorientation, IPF map, textures, and other related microstructural features were obtained from the EBSD data using HKL Channel 5 software. Finally, as shown in the black box in Fig. 1(b), Vickers hardness test was used to evaluate the hardness of the samples. For each sample, ten points were tested and the average value was calculated.

3 Results and discussion

3.1 Effective strain

Figure 2 shows the effective strain distributions in the 2nd pass and 4th pass of three groups. Overall, the effective strain is improved as the number of passes increases. For example, Group C, the average effective strain of the 2nd pass is 0.75, and that of the 4th pass is 1.05. According to the relevant literature [15,16], during continuous bending and flattening of the workpiece, its thickness gradually decreases while its length and width progressively increase. The latter exhibits a more significant increase than the former. This might increase the local relative deformation of the workpiece and result in a higher effective strain. Furthermore, the deformation effect on the workpiece varies depending on the angle of dies used in this process. Group C produces the highest deformation, followed by Group A and then Group B. In the 4th pass, the maximum and average effective strains of Group A are 4.08 and 1.10, while those in Group B are 1.33 and 0.50, and those in Group C are 4.34 and 1.05, as shown in Figs. 2(b, d, f), respectively. Additionally, a load distribution that is homogeneous and huge in the center but dispersed and modest at the periphery could also account for the observation that internal regions are higher than external regions. Finally, regardless of the die or pass, an interval distribution is exhibited by overall effective strain in the flow direction (FD), with high and low strain zones that are close to one another.

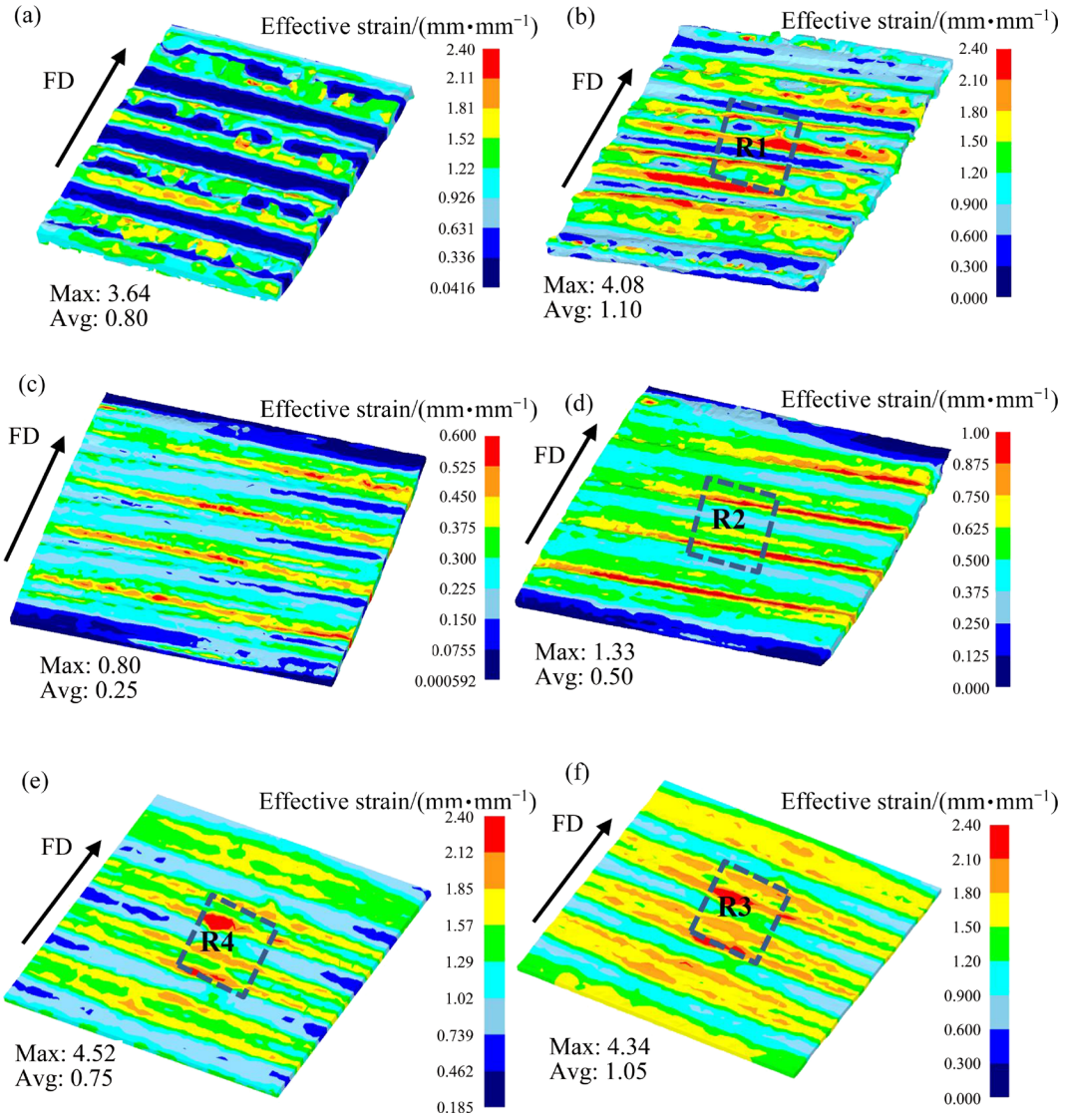

Fig. 2 Strain cloud maps of samples treated by the 2nd and 4th passes: (a) 2nd pass of Group A; (b) 4th pass of Group A; (c) 2nd pass of Group B; (d) 4th pass of Group B; (e) 2nd pass of Group C; (f) 4th pass of Group C

As reported in Refs. [13,14] a larger bending deformation strain is more likely to generate a finer microstructure. Typically, fine grains are found in the high strain regions while coarse grains are found in the low strain regions. Thus, the microstructure in FD may exhibit an interval distribution, both high strain and low strain, and region by region, and microstructure in internal regions is finer than that in external parts. Meanwhile, Group C has the smallest microstructure in our study, and grain size has decreased significantly as the process continues, showing the best grain refinement effect in the three groups. High strain leads to high strain hardening, which permits additional elongation. It is widely known that elongation, particularly UFE, is directly related to the behavior of strain hardening and can be effectively promoted by the smaller grain size resulting from increased strain [15,16]. Group C may exhibit the largest strain hardening ability and the best plasticity. All the above results suggest that the 150°/150° die function may be the best group after a four-pass RBFD process.

3.2 Flow rate

Figure 3 depicts the flow rate distribution in small core slices of the 2nd and 4th passes, which are named R1, R2, R3, and R4 as shown in Fig. 2. Firstly, the flow rate in FD is comparable to effective strain because the way bending dies are built, resulting in an interval distribution with adjacent high-value and low-value parts. Furthermore,

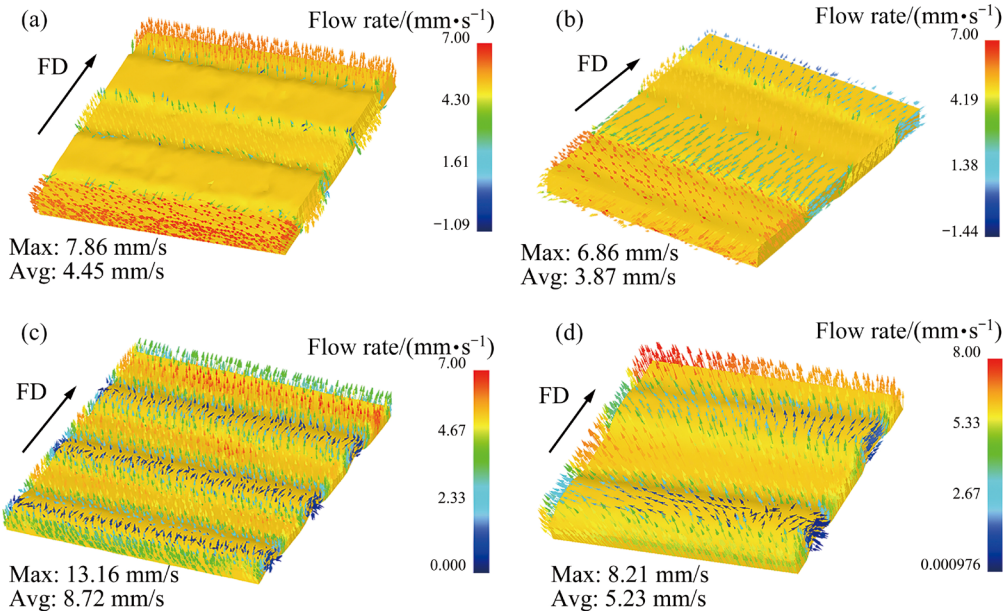

Fig. 3 Flow rate vector maps for different group regions selected in Fig. 2: (a) R1; (b) R2; (c) R3; (d) R4

in Figs. 3(a−c), Group A has a higher flow rate than Group B, but it does not cover the entire workpiece. In contrast, Group C not only has the highest flow rate of 13.16 mm/s but also it is more uniform than any other group. Finally, comparing Figs. 3(c, d), the average flow rate of the 2nd pass reaches 5.23 mm/s, while that of the 4th pass is 8.72 mm/s, showing that the effect of flow rate is increasing with the process operating at the same time.

During the bending of Mg alloys, the magnitudes of surface flow rate and the shear force have a positive correlation, which can be expressed as Eq. (1) below [17,18]:

$$Q=\frac{\mathrm{d}M}{\mathrm{d}x} \tag{1}$$

where Q is the shear force, M is the bending momentum, and x is the displacement. $\mathrm{d}M/\mathrm{d}x$ represents the shear flow rate. The coupling of shear action and bending can activate non-basal slip, dissolve twin, release misorientation and trigger DRX, which is beneficial to grain refinement [19,20]. The more complete the DRX process is, the higher the magnitude of shear force is. As shown in Fig. 3, the vast majority of the flow rates for all samples are directed towards the thickness, and the variation in the FD is negligible. Even though it still exists, the flow rate does not follow the direction of grain thickness, but this influence is slight and helpful for refining the grain. Thus, in contrast to the direction of the flow rate, the value of the flow rate plays a crucial part in that of the shear effect. Based on these findings, Group C has the greatest shear effect, and its impact on grain refinement is similarly variable. With an increase in passes, the shear force also becomes larger as Fig. 3 depicts, resulting in the phenomenon that although the overall distribution is spaced, the grain size decreases both in the coarse and fine grains, suggesting that twins may decrease to promote DRX.

Additionally, WANG et al [21] demonstrated that the intense basal texture was partially attributed to the symmetric shear stress generated by the upper and lower rollers, which aligned the basal poles parallel to the normal direction (ND). However, due to different forces applied on the upper and lower surfaces, shear force acted differently on them, leading to potential changes in crystal orientation and thus weakening the basal texture intensity. The greater asymmetrical the deformation or force exists, the more the changes in crystal orientation occur. Extrusion is similar to rolling in that the force on the top die is different from that on the bottom die, as shown in Fig. 4, and this also leads to different shear effects, resulting in a change of crystal orientation. However, in Group B, there is a difference not only in the shear force distribution between the top and bottom dies but also within each die itself due to varying angles of

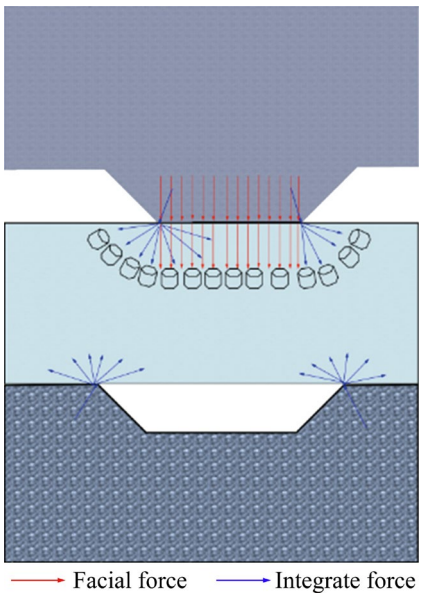

Fig. 4 Schematic illustration showing shear stress during process

individual tooth on the left and right sides, resulting in different forces applied to each tooth. Thus, this theory is not applicable to Group B. Therefore, only Groups A and C conform to it, indicating a good shear force coupling effect on grain refinement and a weak basal texture.

3.3 OM observation

Figure 5 shows the microstructure of fine grain areas (FG area) and coarse grain areas (CG area) after the 4th pass with different die angles. The microstructure exhibits an interval distribution in which coarse and fine grains are adjacent to one another, as expected in the previous sections. Besides, the CG area width in three groups follows a descending order of Groups B, A, and C. This indicates that grain refinement is most effective in Group C. Finally, as seen in Figs. 5(b, d, f) the grain sizes between the largest grain and the smallest one

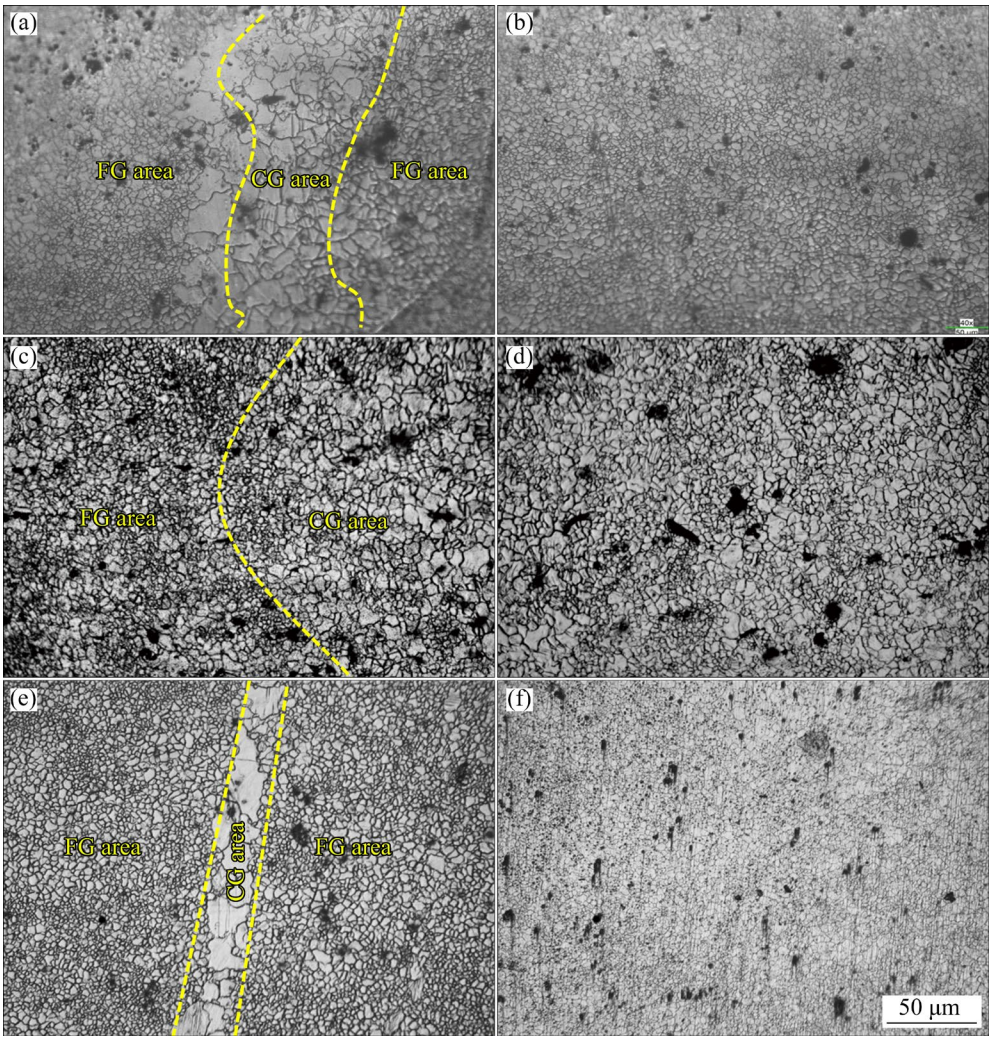

Fig. 5 OM images of different groups in interval grain regions (a, c, e) and fine grain regions (b, d, f): (a, b) Group A; (c, d) Group B; (e, f) Group C

in Group C are 2.7 and 0.7 μm, respectively, those of Group B are 6.2 and 1.8 μm, respectively, and those of Group A are 3.7 and 1.3 μm, respectively, which also reveals that Group C has the smallest grain size and the most homogenous microstructure of the three groups, while Group B is the largest one and Group A is in the middle of the previous two groups.

Figure 6 shows the microstructure of FG area in different passes. The average grain sizes of the 1st, the 2nd, the 3rd, and the 4th passes are 3.3, 2.5, 2.2 and 1.7 μm, respectively, indicating that with the process pushing forward, the grain size is falling. The average grain size of Mg−6Zn−1Gd−1Er has been refined to 15.9 μm by pre-aging hot extrusion, also the average grain size of AZ31B pipes has been refined to 17.1 μm by the extrusion−shear−bending forming method, which was less efficient than our method according to the related literature [7,8]. Exceedingly, the grain refinement and microstructure homogeneity are better in the internal regions of the sample than those in the external sections. This is evidenced by the average grain size increasing from the inside to the outside across four passes, and a corresponding decrease in uniformity.

Unlike FEM, when the punching machine is operated manually, the surface of the die is in touch with the workpiece, and because the pressure applied to the workpiece is not constant during the process, the force on the workpiece's surface is also uneven [17,22]. The internal region near the center of the press experiences greater and more uniform pressure, which may result in obvious refinement and improved uniformity. But, little refinement takes place in the external region where the pressure is lower than that in the internal region and there may even be no-pressure zones where no forces interact, thus creating the difference.

Regardless of the type of dies, the grain size decreases after four passes. This is especially true for Group C, which can be attributed to both the largest local relative deformation and the largest effective strain. CHANG et al [23] and KIM et al [24] also noted that as DRX occurred more completely, the number of twins decreased due to increasing shear force. This suggests that shear force has a positive effect on microstructure characteristics, consistent with the findings in Section 3.2. WANG et al [21] have shown that multi-pass deformation can improve the homogeneity of microstructure by DRX. This can be inferred from the log-normal distribution of

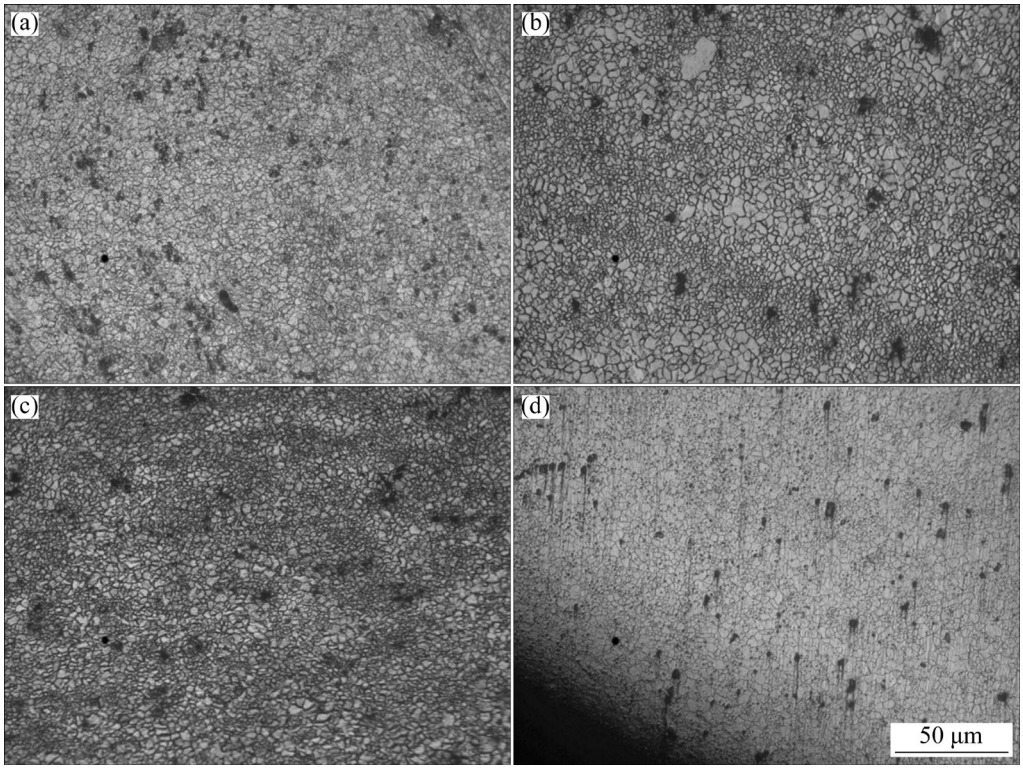

Fig. 6 OM images of fine grain regions of Group C in different passes: (a) 1st pass; (b) 2nd pass; (c) 3rd pass; (d) 4th pass

grain sizes, and the degree of DRX completion is indicated by the peak of three curves. As depicted in Fig. 7(a), DRX may occur, and the DRX of Group C will occur more completely if it exists since the curves fit log-normal distributions and the peak of Group C is at the top of three groups. Similarly, as shown in Fig. 7(b), multiple DRX may occur throughout the process, from the first to the fourth pass, based on the following three points: One way to demonstrate this is by fitting the grain size distribution curves in four passes to log-normal functions. This demonstrates that as the process continues, the peak rises steadily, suggesting a rising proportion of DRX [7,25]. On the one hand, the grain boundary may dissolve and reconstruct DRXed grains while smaller grains (<2 μm) grow within larger grains [16,26]. Finally, Group C has experienced DRX because it has equiaxed grains at various passes, as observed in Figs. 5(e, f) and Figs. 6(a−d), which are consistent with a previous thesis [27] but from a different perspective. Above all, multiple DRX occurrence is highly probable in our process, and the degree of the completeness

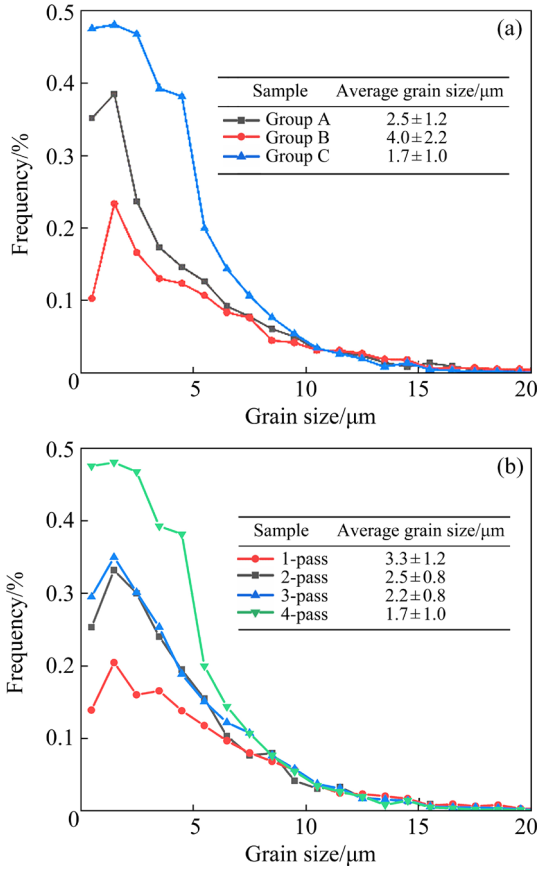

Fig. 7 Grain size distribution maps: (a) Fine grain regions in Figs. 5(b, d, f); (b) 1−4 passes in Figs. 6(a−d), respectively

increases with the pass number. This is advantageous for microstructure characteristics to improve the properties of Mg alloy, which are consistent with previous research findings [7,16]. Especially, according to WANG et al [13,14], more bending can result in finer grains.

3.4 EBSD observation

Figure 8 shows the inverse pole figure (IPF), grain boundary (GB), various twins, and kernel average misorientation (KAM) maps for different groups. Group C has the smallest grain size and the most homogeneous microstructure, without any twins or low angle grain boundaries (LAGBs). Groups A and B also have small grains similar to those observed in OM images, as shown in Figs. 8(a, b, d, e). Even Group B has a maximum grain size about 15 μm. Moreover, although the grain size of Group A is slightly larger than that of Group C, its crystal orientation changes more frequently than that of Group C, with the existence of LAGBs, twins and many non-basal grains in Figs. 8(a, b).

Subsequently, as shown in Fig. 8(i), the majority of specimens in Group C are composed of fine grains with low dislocation densities and a small number of coarse grains with internal areas of low dislocation and high dislocation edges. Fine grain may consist of DRXed grains that cover the majority of specimens with small internal orientation differences and low dislocation density after four passes. Misorientation and energy were consumed too much while twins dissolved, resulting in small residual strain in AZ31 grains under 150°/150° dies, which was only distributed at grain boundaries and in a small number of coarse grains. It is assumed that almost full DRX has occurred without visible LAGBs. Meanwhile, in Group A, only a few grains appeared blue, while most of grains showed green or yellow (Fig. 8(c)). These findings suggest that DRX occurred to a less extent in Group A. Only a few high-angle grain boundaries (HAGBs) are present, indicating that the microstructure may mainly consist of sub-structured grains in Group A. However, Group B not only has a large number of dislocations but also the highest frequency of twins, including numerous $\{10\bar{1}2\}$ tensile twins and a few $\{10\bar{1}1\}$ contraction twins. Additionally, it possesses the largest grain size among the three groups with only

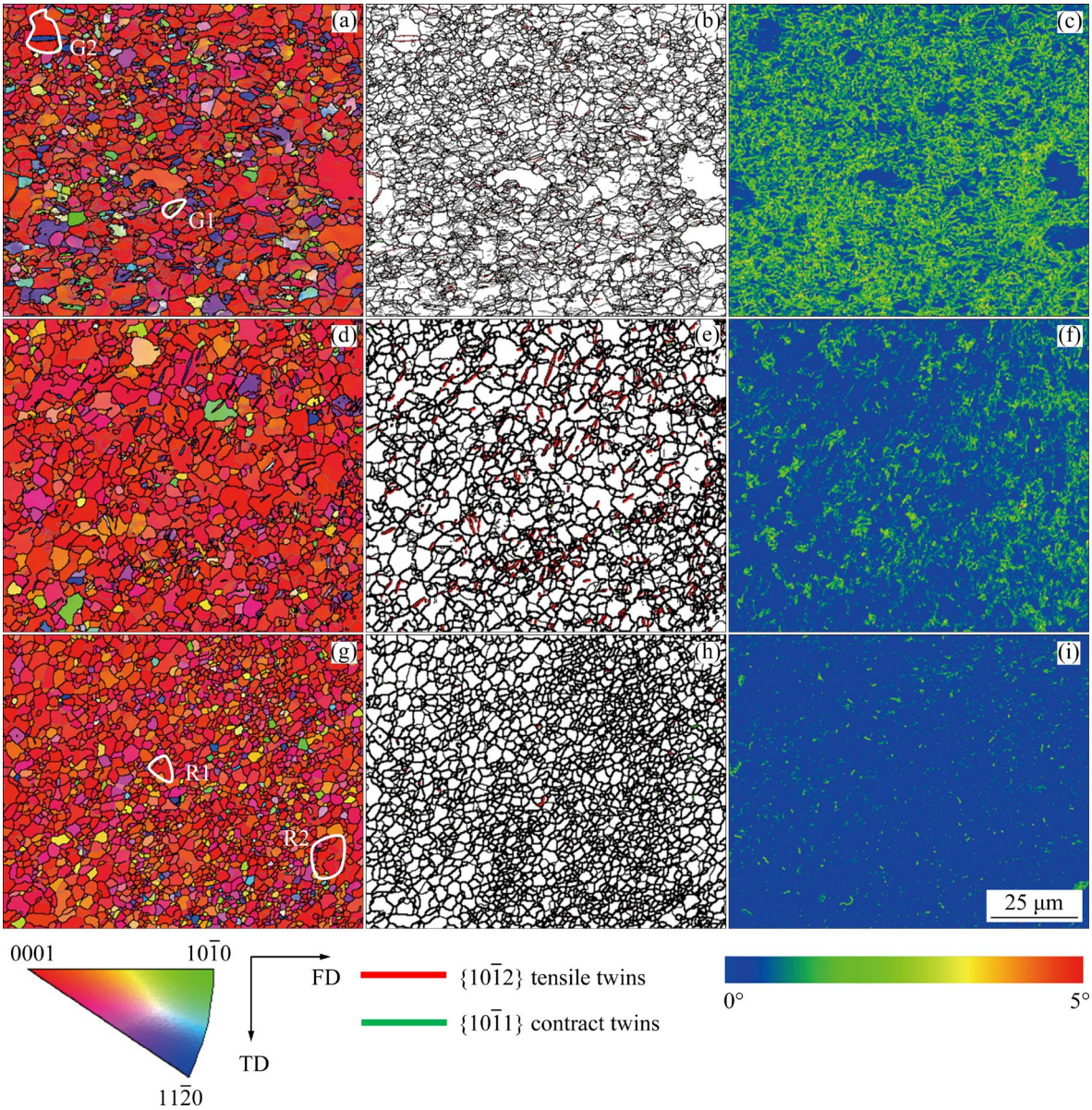

Fig. 8 IPF (a, d, g), GB+twins (b, e, h) and KAM (c, f, i) maps of different groups: (a−c) Group A; (d−f) Group B; (g−i) Group C

a few low-angle grain boundaries (LAGBs), as shown in Fig. 8(e). This suggests that although its grain size is smaller than that of the original sample, almost no dynamic recrystallization occurred and most grains remained deformed.

In order to better visualize the KAM values of the three specimens, the angular distribution of different orientations was obtained by processing the KAM data, and the geometrically necessary dislocation (GND) density was used to predict the total dislocation density, where the GND density can be expressed as Eq. (2) [4,17]:

$$\rho^{\mathrm{GND}}=\frac{2\Delta\varphi}{ub} \tag{2}$$

where ρ^{GND} represents GND density, $\Delta\varphi$ represents average angle of local misorientation, u is the scan step of the EBSD, and b is the amplitude of Burgers vector standing for 3.21×10^{-10} m. We can conclude that the ρ^{GND} for Groups A, B, and C are 1.55×10^{15}, 0.79×10^{15}, and 0.45×10^{15} m^{-2}, respectively. The difference between Group A and Group C is that the ρ^{GND} for former is more than three times greater than that for the latter, demonstrating how the higher level of internal dislocation and misorientation in small angle die conditions impede DRX, which prevents the release of locally concentrated stresses through the formation of a significant amount of DRX. When the die of Group

C acts on the Mg alloy sheets, it makes the DRX process more efficient. As a result, the DRXed grains have a lower dislocation density, which significantly improves the plasticity and strength of the sheet [28].

According to Refs. [22,26,29,30], both twinning and DRX play an important role in microstructure and texture evolution during the RBFD process. To analyze the effects of twinning and DRX under different dies in detail, we conducted a detailed analysis of G1, G2 and R1, R2 as shown in Fig. 8. To demonstrate the ability of twins to modify grain orientation, two grains with single twins were selected for analysis. As shown in Figs. 9(a−c), the *c*-axis of G1 deviated by approximately 50° from near $[\bar{1}2\bar{1}0]$ towards the junction zone between [0001] and $[01\bar{1}0]$, then decreased to around 15° after tensile twinning (TT). Similarly, the single 86.1° $\langle 11\bar{2}0\rangle$ type TT generated in G2 had its *c*-axis increased from 2° to 86° and deviated away

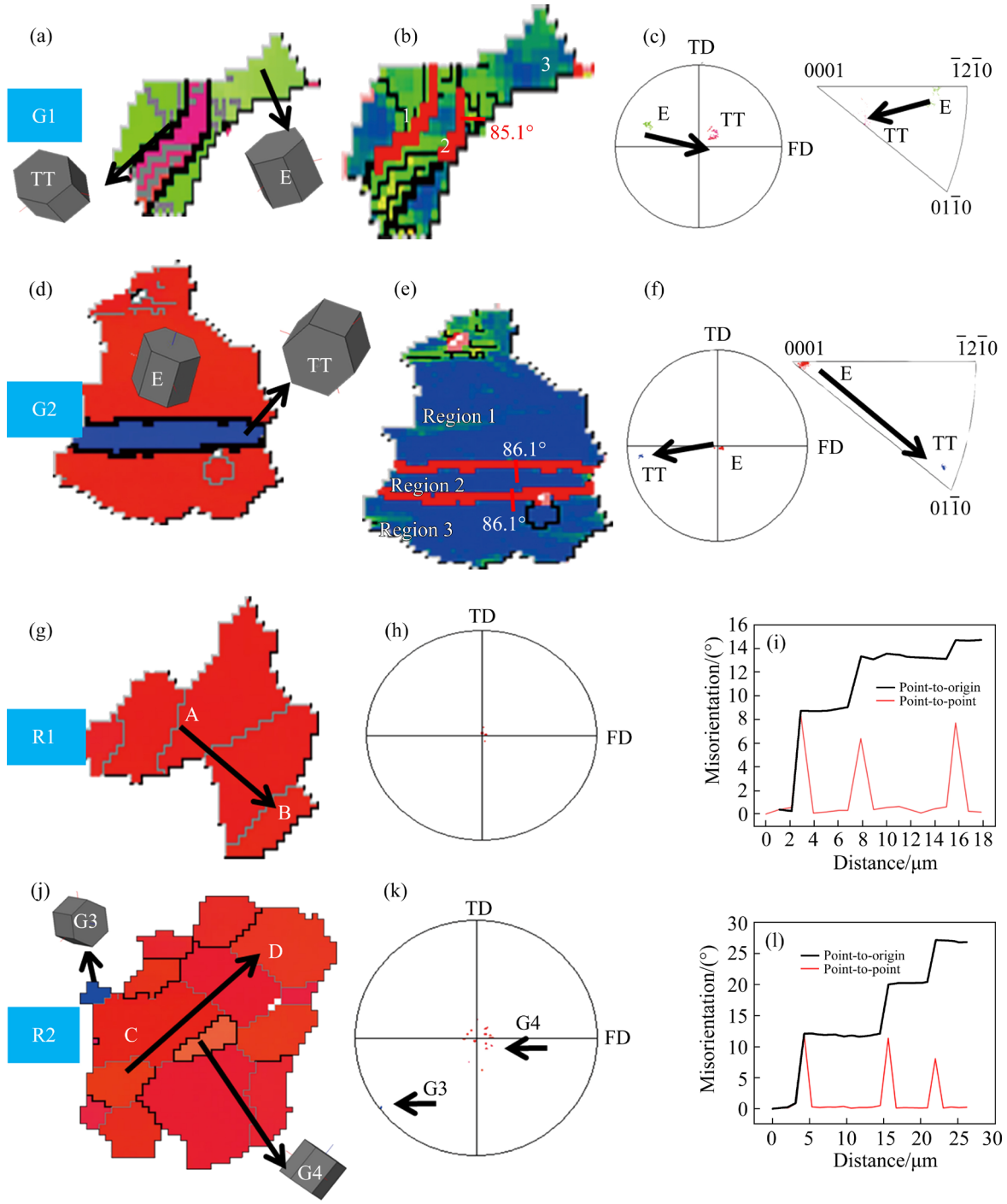

Fig. 9 Twinning behavior and DRX towards microstructure selected in Figs. 8(a, g): (a−c) G1; (d−f) G2; (g−i) R1; (j−l) R2

from [0001] to $[01\bar{1}0]$, as shown in Figs. 9(d−f). Except for altering orientation, twins can also divide grains, which will enhance the resistance to dislocation movement. As shown in Figs. 9(a−c), the $\{11\bar{2}0\}$ TT divides G1 into 1−3 regions. Figures 9(d−f) show that twinning also separates G2 into 1−3 regions. LUO et al [12] and CHE et al [26,28] have also reported these two phenomena.

Two regions were selected for analysis to confirm the occurrence of continuous dynamic recrystallization (CDRX) during the process. As shown in Figs. 9(g, h), R1 is a grain that contains multiple LAGBs that have a tendency to transform into HAGBs as dislocations accumulate. Figures 9(j, k) show a region involving multiple small DRXed grains, such as G4 that is an obvious DRXed grain surrounded by full HAGBs. Its crystal orientation has also changed.

G3 is a sub-grain that is similar to the grain in R1, which has potential to transform into a grain with HAGBs. Similarly, its crystal orientation has changed from red to blue. These phenomena indicate that DRX not only refines grains but also may cause changes in crystal orientation. Finally, the accumulated orientation angle increases as shown in Figs. 9(i, l), indicating that CDRX is the dominant type of DRX occurring in RBFD without a clearly defined nucleation and growth stage [3,22]. Notably, Group A exhibits numerous LAGBs with larger KAM values and misorientations around internal regions and boundaries of $\{11\bar{2}0\}$ tensile twinning compared to other groups. The LAGBs can easily transform into HAGBs, thereby promoting the DRX occurrence [12]. This may demonstrate that Group A has the potential to further refine, as there are still many twins and the DRX has not fully occurred. Additionally, the fact that LAGBs cover a large area indicates that CDRX has not been completed and there is potential for further grain refinement [22,28].

It has been mentioned that a twin boundary can also be utilized to prevent dislocations from shifting, which has the added advantage of significantly refining the grains. According to ZHAO et al [31], increasing the twin density in Mg alloys improves their ability to resist dislocation migration during plastic deformation, thereby enhancing the strength of the alloy. Additionally, the Lomer−Cottrell lock and springing strength are effective ways to prevent dislocation sliding when they accumulate at twinning boundaries and induce stress concentration [32,33]. Finally, twins can successfully separate the grains even further to enhance resistance to dislocation movement [34], which increases the Taylor index and demonstrates that grain refinement significantly strengthens Mg alloys [35].

Except for twinning behavior and DRX, grain refinement of Mg alloys is also influenced by non-basal slips. In this study, Schmid factor (SF) analysis was employed to intuitively evaluate the activities of slip during deformation along various loading directions at ambient temperature. According to WANG et al [7,16], a slip with a higher SF value would be more easily activated. The following equation can be used to calculate the SF value for a specific deformation mechanism:

$$\mathrm{SF}=\cos\alpha\cdot\cos\beta \tag{3}$$

where α represents the angle between the normal plane of slip mode and the loading direction, and β represents the angle between the shear direction of slip mode and the loading direction.

Figure 10 shows the SF values of different slip systems of Group C during the 4th pass. As depicted in Fig. 10, the average SF values range from 0.41 to 0.09, with pyramidal $\langle c+a\rangle$ slip having the highest value and prismatic slip having the lowest value, followed by basal slip and pyramidal $\langle a\rangle$ slip. This suggests that pyramidal $\langle c+a\rangle$ slip may be more frequently activated throughout the entire system, resulting in a dispersed and weaker basal texture that has potential for improving elongation. The higher the SF value is, the easier it is to activate under the same external force and plastic deformation. The essence of slip is the movement of dislocations, which is hindered by grain boundaries due to the irregular arrangement of atoms and large distortions [17]. Grain boundaries also have the ability to adsorb various impurity elements, further obstructing the dislocation movement. Additionally, dislocation movement is often influenced by grain size; smaller grains result in a higher number of grains per unit volume and can reduce dispersion in larger grains [3]. Thus, grain refinement increases the dislocation slip distance and shortens the length of dislocation plugging groups, thereby reducing stress concentration near grain boundaries. This is beneficial to activating pyramidal $\langle c+a\rangle$ slip and enhancing plasticity [36].

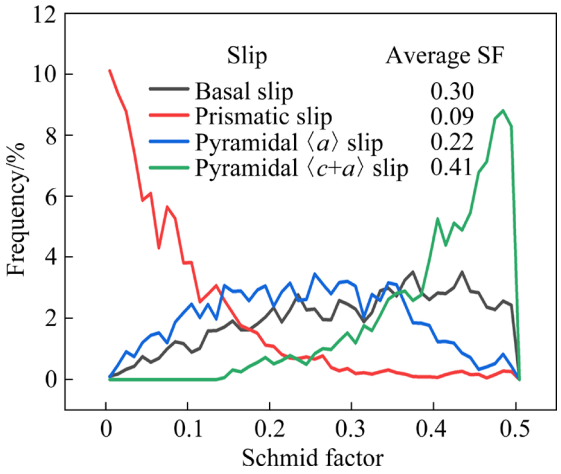

Fig. 10 Schmid factor (SF) map of statistical graph of four slip systems

Non-basal slips, especially pyramidal ⟨*c*+*a*⟩ slip, are significant for SPD. They play a crucial role in the plastic deformation of HCP metals, not only for understanding dislocation mechanisms but also for designing and processing alloys. On the one hand, pyramidal ⟨*c*+*a*⟩ slip provides five independent slip systems, particularly in the $\langle 11\bar{2}3\rangle$ direction, which can coordinate deformation along the *c*-axis and fully satisfy the von-Mises criterion [3,36]. On the other hand, the primary non-basal slip mode in HCP metals is known as pyramidal ⟨*a*⟩ or prismatic ⟨*a*⟩ slip. Basal and prismatic ⟨*a*⟩ slip systems only cause strain in the ⟨*a*⟩ direction. By adding a strain component along the ⟨*c*⟩ direction, the activation of pyramidal ⟨*c*+*a*⟩ slip can improve deformation homogeneity. The first-order $\{10\bar{1}1\}\langle 11\bar{2}3\rangle$ mode and the second-order $\{\bar{1}\bar{1}22\}\langle 1123\rangle$ mode are two main modes of the pyramidal slip that affect the ductility of HCP metals significantly [3,37].

Based on the above two, under 4 passes conditions, we can conclude that the largest SF value slip of Group C, pyramidal ⟨*c*+*a*⟩ slip, could elongate in the ⟨*a*⟩ direction, thereby improving deformation homogeneity and ductility. Furthermore, the SF value of basal slip is larger than that of prismatic and pyramidal ⟨*a*⟩ slips. Basal slip may occur less frequently than pyramidal ⟨*c*+*a*⟩ slip but more often than the other two types, which has a beneficial effect on retaining some basal texture intensity and improving strength. In other words, Group C not only improves the plasticity of Mg alloy but also slightly intensifies its strength.

Figure 11 depicts the pole figure (PF) of the (0001) plane in different groups. In the (0001) PF, Group B obtains a concentrated distribution with a maximum intensity of 17.20, which is the largest among all groups. Meanwhile, as shown in Fig. 11(a), Group A exhibits a bimodal texture and is uniformly dispersed into two regions with a maximum intensity of 11.61. Group C falls between the previous two groups with a maximum intensity of 12.84 but remains in one. The basal textures of Groups A and C disperse, homogenize, and weaken, which may be beneficial to improving plasticity [18]. The key question is which process contributes the most, since grain refinement often improves both plasticity and strength, while texture weakening may increase plasticity but decrease other properties [3,7,13]. Given that Group C has the smallest cloud size and its basal intensity is close to that of Group A, inferring that Group C has the highest plasticity. From the previous section, Group A has plenty of LAGBs with twins while Group C is full of HAGBs with few twins. This indicates that the microstructure of Group A has potential for further refining through CDRX, whereas Group C may not have room for further refinement. Thus, we confirm that Group A may

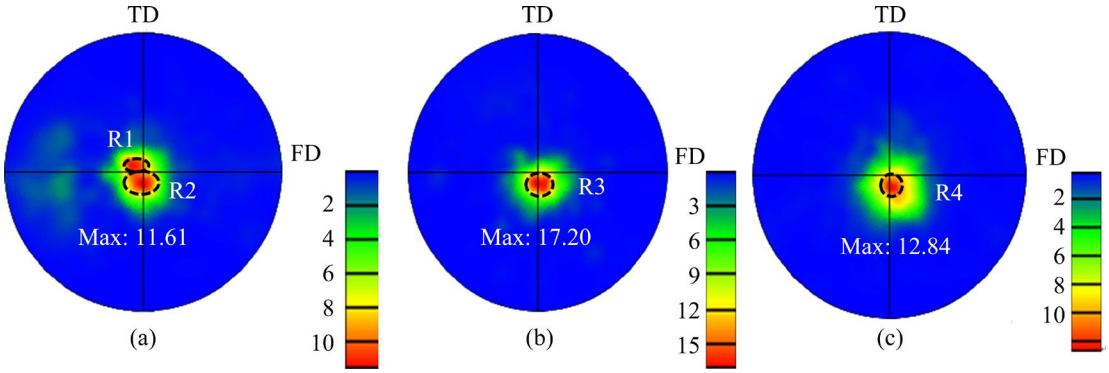

Fig. 11 (0001) pole figures of different groups in 4th pass: (a) Group A; (b) Group B; (c) Group C

result in a smaller grain size than Group C after more passes. Additionally, the basal texture of Group A developed into a bimodal texture after 4 passes, as shown by R1 and R2 in Fig. 11(a). Furthermore, if the process continues, Group A may also form a non-basal plane strengthening texture, due to its diversity, two stronger peaks may occur [3].

Basal texture weakening may be owed to the non-basal slip. When more frequent non-basal slips are activated in the slip system, more uniform and weaker basal texture will become [8]. Combining the results depicted in Fig. 10 shows that frequent activation of pyramidal ⟨*c*+*a*⟩ slip weakens the basal plane texture, decreases UTS and YTS, while increases UFE. Meanwhile, refined grains makes UTS, YTS, and UFE increase sharply [25,38], demonstrating that high plasticity can be achieved through bending SPD more effectively than other techniques. Meanwhile, based on the results and discussion in Fig. 9, it is certain that the texture characterization is strongly related to the twinning behavior and DRX during the process.

Figure 12 displays inverse pole figures, (0001) pole figures, and SF distribution maps of the main principal grains of R1−R4 selected in Fig. 11 to further investigate the mechanism of texture weakening. The *c*-axis of the major distorted grains in R1 and R2 tilted roughly 0°−10° and 0°−15° away from ND towards TD, as shown in Figs. 12(a, c). The distribution and average SF values of R1 and R2 slip systems are shown in Figs. 12(b, d). The SF values of the pyramidal ⟨*c*+*a*⟩ slip has the highest proportion in the range of 0.45−0.5, as can be seen in Figs. 12(b, d). The average SF value of basal slip of the major grains of R1 is 0.20, while it is 0.47 for pyramidal ⟨*c*+*a*⟩ slip, indicating that dislocations with pyramidal ⟨*c*+*a*⟩ slip have a higher active ability. Similarly, the average SF value of the major grains of R2 pyramidal ⟨*c*+*a*⟩ slip is also higher than any other slip, indicating that pyramidal ⟨*c*+*a*⟩ slip dislocation activation is more prevalent. Pyramidal ⟨*c*+*a*⟩ slip was easily observed in an aged precipitation hardening alloy, as reported by ALIZADEH et al [27]. According to ZECEVIC et al [37], when the pyramidal ⟨*c*+*a*⟩ slip is reoriented, the peak texture in TD becomes skewed. As a result of frequent activation of this slip system, R1 and R2 individually deflect from ND to each side of TD, forming a bimodal texture. HAN et al [39] reported a similar rationale for the double-peak basal texture. Similarly, although the *c*-axis of major distorted grains of R3 tilts 0°−12° from ND to TD, basal slip is sufficiently activated that the average SF value is 0.47, whereas pyramidal ⟨*c*+*a*⟩ slip and other non-basal slips are less than 0.20, as shown in Figs. 12(e, f). This indicates that non-basal slips are not sufficiently activated, which may explain why Group B has the highest intensity and most concentrated basal texture among all three groups, as shown in Fig. 11(b). Finally, the *c*-axis of major distorted grains of R4 tilts 0°−13° from ND to TD. Although pyramidal ⟨*c*+*a*⟩ slip is also prominent, its average SF value of 0.45 is lower than that of R1 and R2. However, its basal slip average SF value of 0.22 is higher than that of R1 and R2. This indicates that the effect of weakening basal texture on R4 is less pronounced compared to R1 and R2, which explains why Group C has slightly greater basal texture intensity than Group A as shown in Figs. 11(a, c).

To further analyze the microstructure and texture evolution, we made scattered PF maps of various slip systems, as shown in Fig. 13. It is well known that the loading direction has a direct influence on the initial texture of Mg alloy sample, as shown in Eq. (3), which further affects the activities of slip modes during plastic deformation [7,16]. This is the fundamental cause of the observed phenomena in terms of mechanical response, microstructure evolution, and texture characteristics.

As observed in Fig. 13, regardless of the die angles, pyramidal ⟨*c*+*a*⟩ slip has the largest SF value after 4 passes in the core region, followed by basal slip, pyramidal ⟨*a*⟩ slip and prismatic ⟨*a*⟩ slip. The combination of the results in Fig. 10 may explain why all three groups obtained smaller grains than the originals. Non-basal slips activate more frequently, especially pyramidal ⟨*c*+*a*⟩ slip, providing five independent slip directions including *c* dislocation that can coordinate deformation with dislocations. This not only reduces grain size but also triggers CDRX to enhance the anisotropy of microstructure [3,36]. Furthermore, all SF distributions of Group A extend in two opposite directions in TD, while the other two are more focused in the core region, and Group B is more concentrated than Group C. ALIZADEH et al [27]

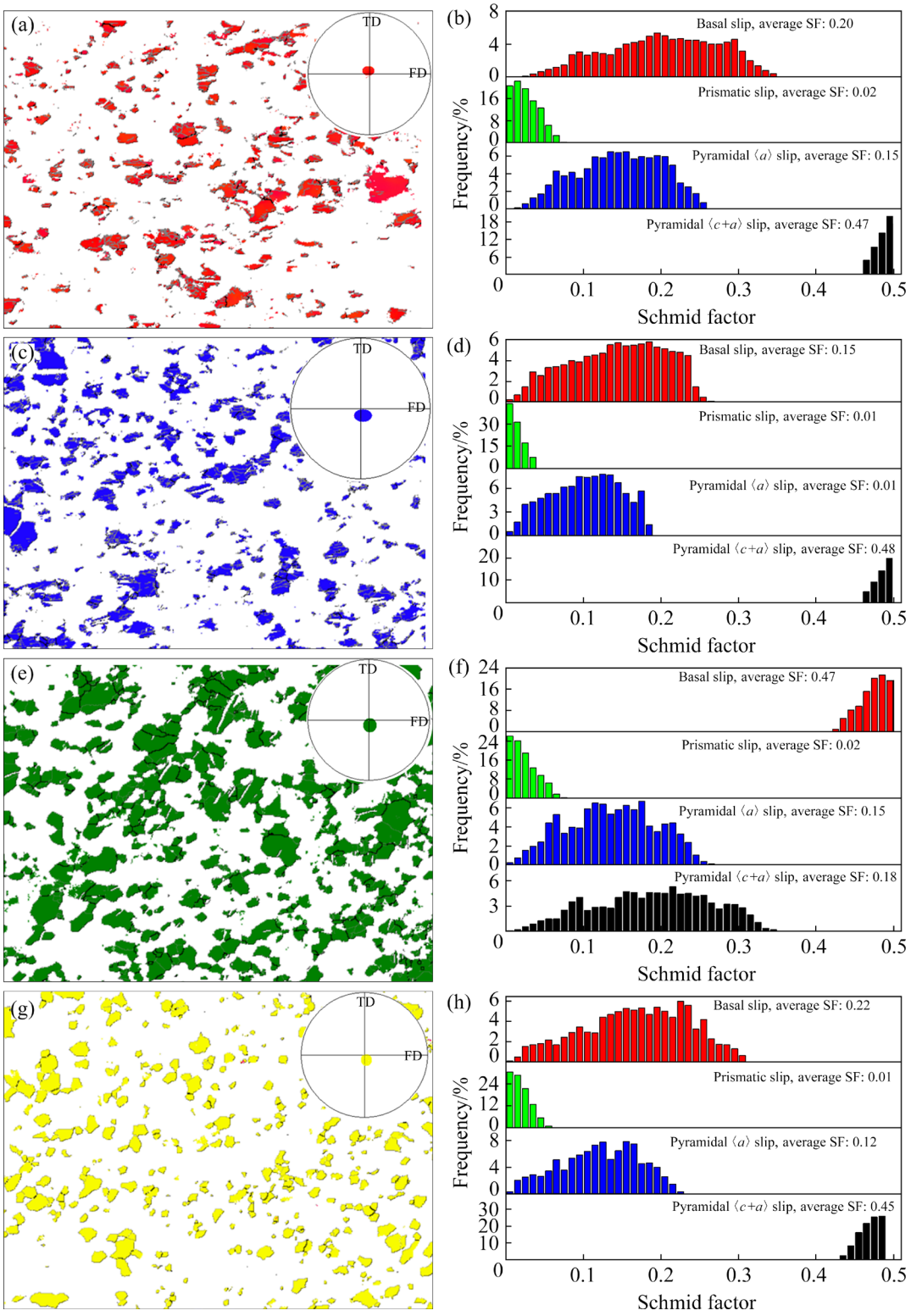

Fig. 12 IPF map, (0001) pole figures and SF distribution map of main grains in R1 (a, b), R2 (c, d), R3 (e, f), and R4 (g, h) selected in Fig. 11

also have established that the huge activation of pyramidal ⟨*c*+*a*⟩ slip can cause the rotation of grain *c*-axis in the direction of a plane almost perpendicular to FD. Thus, it is clear why Group A has a bimodal basal texture and the basal texture of Group C is weaker than that of Group B. Additionally, the SF value of prismatic slip is near 0 in the core region of all three groups, demonstrating

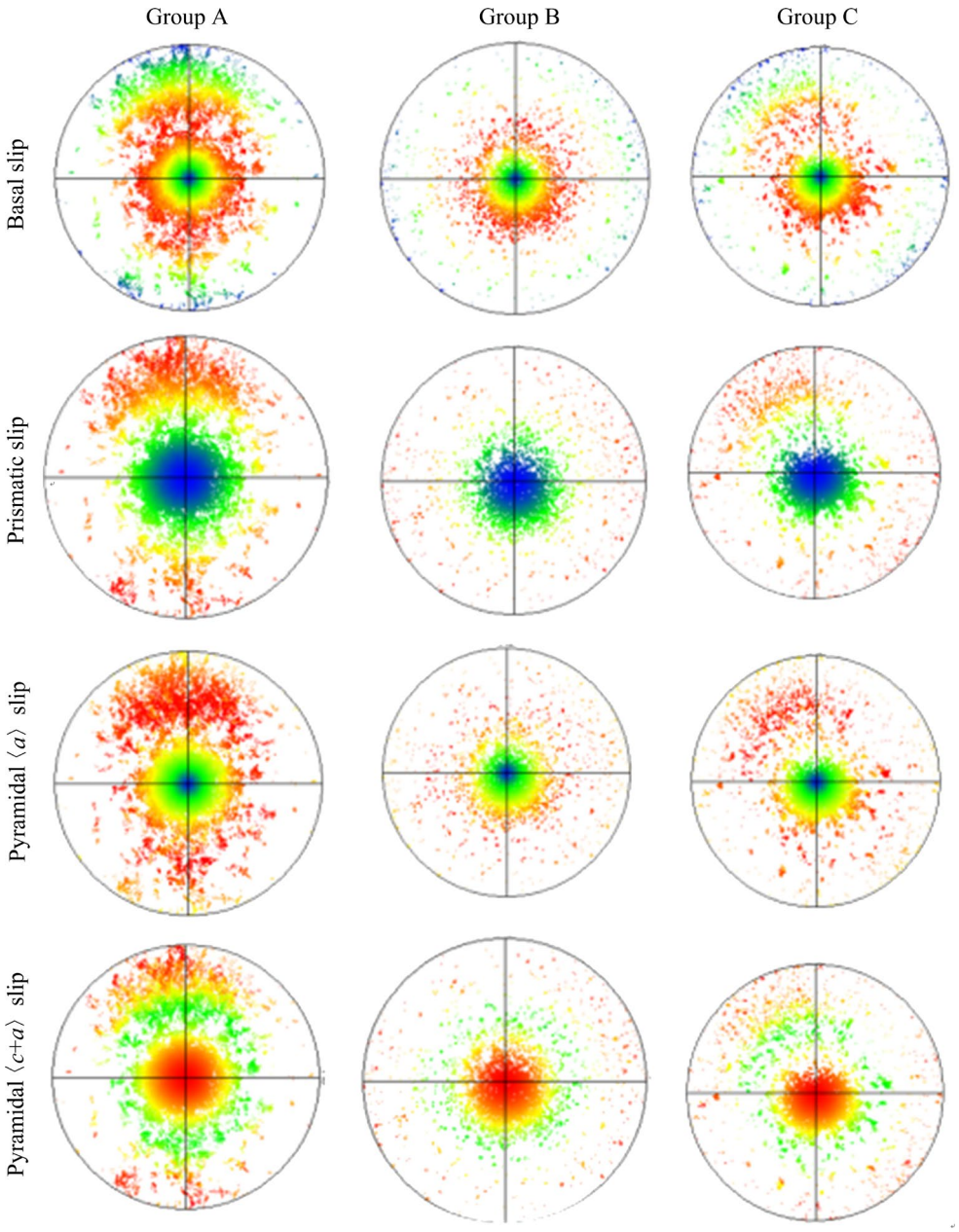

Fig. 13 Scattered distributions of various slip SF values (basal ⟨*a*⟩ slip, prismatic ⟨*a*⟩ slip, pyramidal ⟨*a*⟩ and pyramidal ⟨*c*+*a*⟩ slip) in three groups

that it may not influence deformation. Finally, accommodating plastic strain between different grains could be challenging due to the fact that pyramidal ⟨*c*+*a*⟩ slip is known as the primary deformation process in all samples. As a result, even if their SF values are fairly low, additional deformation mechanisms, such as $\{10\bar{1}2\}$ tensile twins, could be engaged to address this issue. SUN et al [40] and RUAN et al [41] have also reported this occurrence.

To investigate the microstructure and texture evolution of Group C more deeply under the RBFD process, samples from the 1st to the 4th passes were selected for EBSD testing, in addition to three samples from various groups in the fourth pass.

Figure 14 shows the IPF, GB, various twins, and recrystallized fractions in different passes of Group C. As observed, the grain size decreases with each pass, resulting in an average size reduction from 3.3 to 1.7 μm. Furthermore, the homogeneity of the microstructure has improved. It is obvious that the size differences between small and large grains are reduced as the process progresses. At the same time, frequent changes in crystal orientation

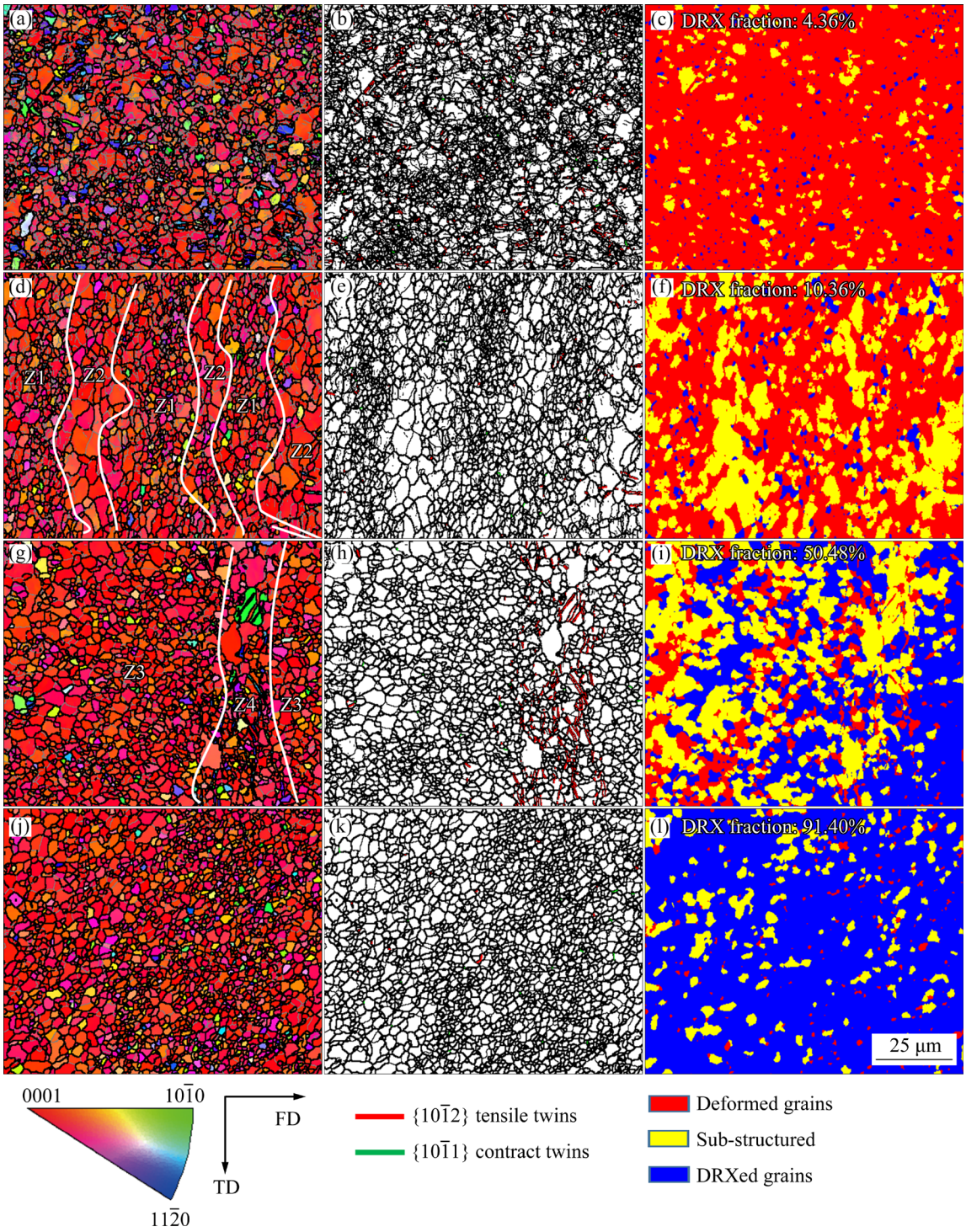

Fig. 14 IPF (a, d, g, j), GB + twins (b, e, h, k) and DRX (c, f, i, l) maps of Group C in different passes: (a−c) 1st pass; (d−f) 2nd pass; (g−i) 3rd pass; (j−l) 4th pass

cause more and more grains to turn from [0001] to [11$\bar{2}$0] or [10$\bar{1}$0], resulting in the appearance of non-basal oriented grains that may even be perpendicular to the ND direction, thus weakening the basal texture. Finally, as illustrated in Figs. 14(b, c, e, f, h, i, k, l), the fraction of DRXed grains increases concurrently with the decline of twins. This is consistent with earlier references [3,16], which demonstrates that the more adequate occurrence of DRX leads to fewer twins in the microstructure. Surprisingly, the fraction of DRXed grains in the 4th pass increases to 91.40%, indicating almost complete occurrence of DRX as demonstrated in the preceding section.

Figure 15 depicts the PFs of the (0001) plane in different passes. It can be observed that the texture distribution becomes increasingly dispersed, and its intensity gradually decreases from 16.84 to 12.84, which is beneficial to ductility [12]. The more the non-basal slips occur in the slip system, the weaker the basal texture will appear [3,16], especially with regard to pyramidal $\langle c+a \rangle$ slip effects during deformation. As we can see, the microstructure distribution of the 2nd pass, which is the middle stage of the process, is an interval distribution that can be divided into two kinds of zones as shown in Fig. 14(d), consistent with previous descriptions in effective strain, flow rate, and OM sections. In Zone 1 (Z1), there are almost fine grains (fine grain regions) with a vast majority of LAGBs and few twins, which may have undergone DRX at that moment. Zone 2 (Z2) mainly consists of coarse grains (coarse grain regions), which is characterized by a few LAGBs and more twins. These features indicate that DRX may also have occurred in Z2, but the effect in Z2 is weaker than that in Z1. The above phenomena demonstrate that different degrees of grain refinement may occur in various positions of the same workpiece under the same pass, due to the structure of the die and load distribution. Additionally, activation of non-basal slips, twinning behavior, and DRX can also vary greatly [42].

Furthermore, to investigate whether twins, especially $\{10\bar{1}2\}$ tensile twins, can also weaken basal texture, two other zones were chosen for analysis. Zone 4 (Z4) has a large majority of $\{10\bar{1}2\}$ tensile twins surrounded by much mis-orientation and misalignment at grain boundaries, as shown in Fig. 16(a), waiting for DRX to continue. Zone 3 (Z3) contains few twins, as illustrated in Fig. 16(c), and DRX occurrence is complete. The basal texture of Z4 is loosely distributed, with an intensity reaching 10.46. A small portion of the texture that has deviated to the edge from [0001] to $[11\bar{2}0]$, as indicated by the red boxes in Fig. 16(b), may gradually transform into non-basal texture, resulting in a high-intensity region deviating from the pole. With an intensity of 18.10, the distribution of Z3 is more centered than that of Z4, and the high-intensity region remains centered near the pole, as shown in Fig. 16(d). As reported in Ref. [29], the twinning behavior may trigger basal texture to turn into non-basal texture and weaken intensity to enhance the plasticity.

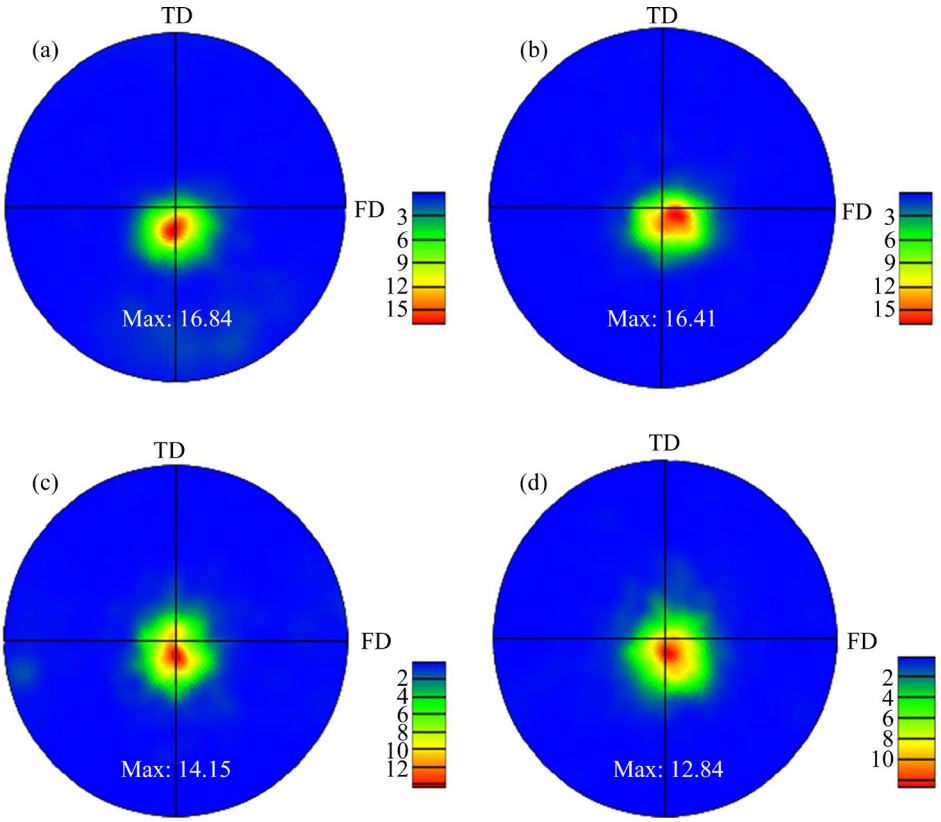

Fig. 15 Pole figures of different passes in Group C: (a) 1st pass; (b) 2nd pass; (c) 3rd pass; (d) 4th pass

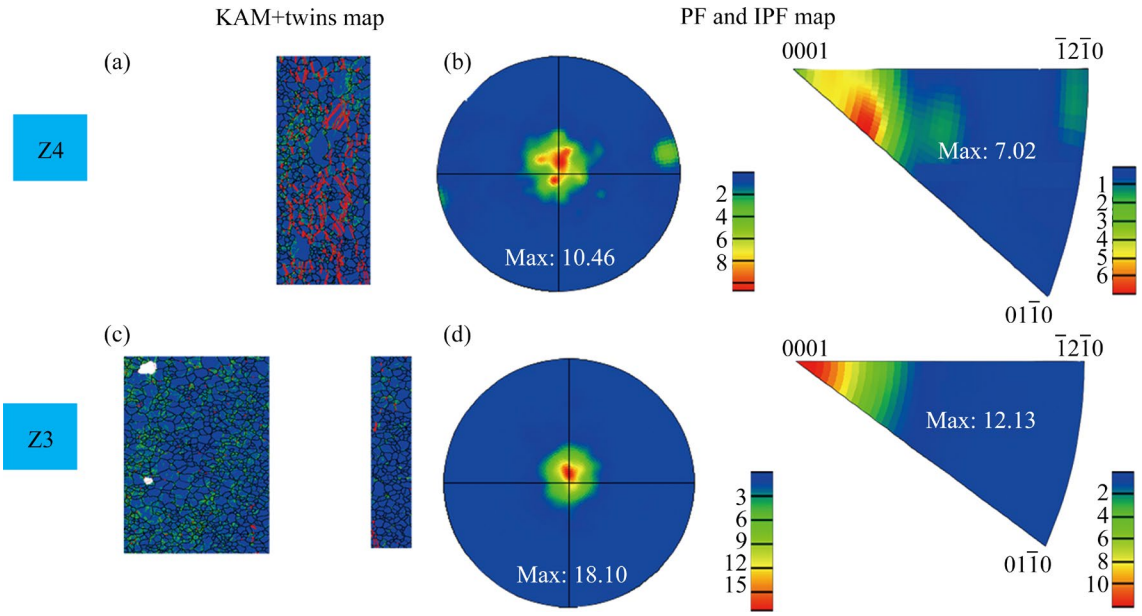

Fig. 16 Twinning behavior effects of Z4 (a, b) and Z3 (c, d) towards weakening basal texture selected in Fig. 14

3.5 Hardness

Figure 17 shows the hardness values from the edge to the center of both the original sample and 4-pass samples in different groups after RBFD. Overall, all three groups exhibit an increase in hardness compared to the original sample, although Group B only shows slight improvements. Moreover, Group C exhibits the highest maximum and average hardness of HV 77.00 and HV 74.46, respectively, indicating an improvement in hardness homogeneity.

According to previous studies [25,38,43] and the above results, hardness is determined by microstructure and texture characteristics. In one aspect, smaller grain size leads to more uniform microstructure and improves strength and plasticity. According to the Hall−Petch relationship of Eq. (4), fine grain strengthening is an effective way to enhance the hardness of the alloy [28]. The material's hardness is inversely related to its grain size, the smaller the grain size, and the higher the hardness. Mg alloys have a higher Taylor index than other types of alloys, so grain refinement has a stronger strengthening effect on them [36].

$$\sigma_s=\sigma_0+kd^{-1/2} \quad (4)$$

where σ_s, σ_0, k and d represent the yield limit, the lattice friction resistance, the Hall−Petch slope and the average grain size of the material, respectively. It should be noted that the value of k is greatly influenced by the number of slip systems in an alloy. The HCP structure, with fewer available slip systems, generally corresponds to a greater value than the body-centered cubic (BCC) or face-centered cubic (FCC) structures [3,36]. As a result, Group C has the smallest grain and the most uniform microstructure in the experiment, which resulted in the most significant enhancement effect on hardness. Thus, texture becomes another decisive factor owing to dislocation movements [43,44]. Group C has a weak basal texture that is somewhat similar to Group A due to frequent dislocation movement, twinning behavior, non-basal slips and competition of DRX. These are the second factors related to enhancing hardness [44]. TIAN et al [45]

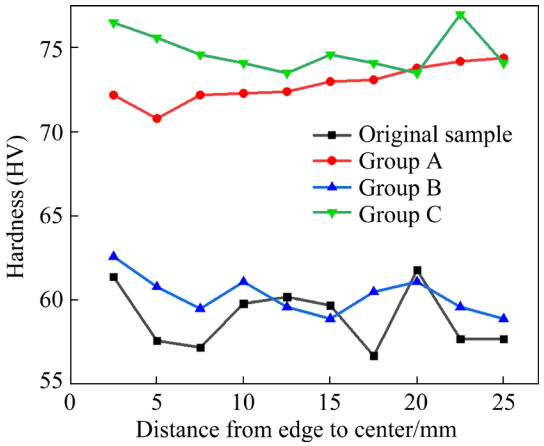

Fig. 17 Hardness values from edge to center of original sample and 4-pass samples in different groups after RBFD

have proven that the hardness has a threefold connection with YTS and UTS, indicating that hardness can partially characterize strength. Therefore, Groups A and C exhibit improved strength properties after 4-pass deformation.

4 Conclusions

(1) The AZ31 magnesium alloy sheet produced in this experiment by the 150°/150° die exhibits the best grain refinement, while the 120°/120° die has potential for further refinement.

(2) The effective strain is improved as the process progresses. The distribution of the effective strain along FD matches with the microstructure distribution, because DRX is activated and twins are dispersed by a combination of shear and bending action.

(3) The average grain size can be significantly refined to 1.7 μm, and a weak basal texture has been obtained after 4 passes, owing to slip, DRX, and twinning behavior. In particular, the pyramidal $\langle c+a \rangle$ slip may happen more frequently, which is beneficial to the grain refinement and texture weakening.

(4) The hardness can reach HV 77.00, revealing the best hardness property of the experiment, enhanced by the competition of microstructure characteristics and texture, which is due to large strain distribution and the high geometrically necessary dislocation.

CRediT authorship contribution statement

Min-hao LI: Conceptualization, Data curation, Formal analysis, Investigation, Methodology, Software, Supervision, Writing − Original draft, Validation, Writing − Review & editing; **Li-wei LU:** Conceptualization, Investigation, Methodology, Project administration, Resources, Validation, Writing − Review & editing; **Yu-tian FAN:** Conceptualization, Data curation, Formal analysis, Investigation, Methodology, Software, Supervision; **Min MA:** Conceptualization, Investigation, Methodology, Project administration; **Zhi-qiang WU:** Conceptualization, Investigation, Methodology, Resources; **Tao ZHOU:** Conceptualization, Data curation, Investigation, Methodology; **Fu-gang QI:** Conceptualization, Investigation, Methodology, Validation, Software; **Hua ZHANG:** Conceptualization, Investigation, Methodology, Project administration.

Declaration of competing interest

The authors declare that they have no known competing financial interests or personal relationships that could have appeared to influence the work reported in this paper.

Acknowledgments

This work was partly supported by the National Natural Science Foundation of China (Nos. 52174362, 51975207), the Xiangtan Special Project for Building a National Innovative City, China (No. CG-YB20221043), and the Yancheng “Talent Plan of Yellow Sea Pearl” for Leading Talent Project, China.

References

[1] XIE He, WU Guo-hua, ZHANG Xiao-long, LI Zhong-quan, LIU Wen-cai, ZHANG Liang, SUN Bao-de. Microstructural evolution and mechanical performance of cast Mg−3Nd−0.2Zn−0.5Zr alloy with Y additions [J]. Transactions of Nonferrous Metals Society of China, 2022, 32(10): 3222−3237.

[2] FAKHAR N, SABBAGHIAN M. Hot shear deformation constitutive analysis of fine-grained ZK60 Mg alloy sheet fabricated via dual equal channel lateral extrusion and sheet extrusion [J]. Transactions of Nonferrous Metals Society of China, 2022, 32(8): 2541−2556.

[3] CHEN Zhen-hua. Magnesium alloy [M]. Beijing: Chemical Industry Press, 2004. (in Chinese)

[4] ZHANG Jia-long, LU Lu-wei, CHE Bo, LI Min-hao, MA Min, YANG Yan. Effects of cryogenic treatment to microstructure and mechanical properties of Mg alloy under variable paths rolling [J]. The Chinese Journal of Nonferrous Metals, 2022, 32(11): 3280−3293. (in Chinese)

[5] LI Xin, LIU Chen, WANG Jun-sheng, ZHANG Chi. Tailoring the strength and formability of Mg alloys through rare earth element additions (Gd and Dy) and dynamic recrystallizations [J]. Materials Today Communications, 2021, 28: 102627.

[6] RAHMANI K, MAJZOOBI G H, EBRAHIM-ZADEH G, KASHFI M. Comprehensive study on quasi-static and dynamic mechanical properties and wear behavior of Mg−B_4C composite compacted at several loading rates through powder metallurgy [J]. Transactions of Nonferrous Metals Society of China, 2021, 31(2): 371−381.

[7] WANG Wen-ke, ZHANG Wen-cong, CHEN Wen-zhen, YANG Jian-lei, ZHANG Lin-xin, WANG Er-de. Homogeneity improvement of friction stir welded ZK61 alloy sheets in microstructure and mechanical properties by multi-pass lowered-temperature rolling [J]. Materials Science and Engineering: A, 2017, 703: 17−26.

[8] KANG Wei, LU Li-wei, FENG Long-biao, LU Feng-chi, GAN Chun-lei, LI Xiao-hui. Effects of pre-aging on microstructure evolution and deformation mechanisms of hot extruded Mg−6Zn−1Gd−1Er Mg alloys [J]. Journal of Magnesium and Alloys, 2023, 11(1): 317−328.

[9] SHENG Kun, LU Li-wei, XIANG Yao, MA Min, WU Zhi-qiang. Crack behavior in Mg/Al alloy thin sheet during hot compound extrusion [J]. Journal of Magnesium and Alloys, 2019, 7(4): 717−724.

[10] WU Hai-rong, DU Wen-bo, LI Shu-bo, LIU Ke, WANG Zhao-hui. Microstructure and mechanical properties of AZ31 magnesium alloy reinforced by *I*-phase [J]. Rare Metals, 2019, 38(8): 733−738.

[11] KIM H K, KIM W J. Microstructural instability and strength of an AZ31 Mg alloy after severe plastic deformation [J]. Materials Science and Engineering: A, 2004, 385: 300−308.

[12] LUO Jun, YAN Hong, LU Li-wei, CHEN Rong-shi, WU An-ru, YIN Fu-cheng. Cold rollability improvement by twinning and twin−slip synergy in an Mg−Zn−Gd alloy with rare earth texture [J]. Journal of Alloys and Compounds, 2021, 883: 160813.

[13] WANG Zhong-tang, WU Kai-qi, ZHANG Hong-liang, LI Yan-juan, LIANG Hai-cheng. Experimental study on progressive compression bending of AZ31 magnesium alloy grid panel [J]. Hot Working Technology, 2023, 52(3): 88−91. (in Chinese)

[14] WANG Zhong-tang, WU Kai-qi, WANG Min-hao, YANG Jun-bao, LIANG Hai-chen. Study on dynamic recrystallization and microstructure evolution of magnesium alloy in process of composite deformation [J]. Hot Working Technology, 2021, 50(19): 94−98. (in Chinese)

[15] ANANT SAGAR D B, PARDHU Y, RAO M S K, NARASAIAH N. Strain hardening behavior of friction welded beta titanium alloy Titan 1023 used for aeronautical applications [J]. Materials Today: Proceedings, 2022, 57: 687−692.

[16] WANG Wen-ke, ZHANG Wen-cong, CHEN Wen-zhen, CUI Guo-rong, WANG Er-de. Effect of deformation temperature on texture and mechanical properties of ZK60 magnesium alloy sheet rolled by multi-pass lowered-temperature rolling [J]. Materials Science and Engineering: A, 2018, 712: 608−615.

[17] HEARN E J. Mechanics of materials 1: An introduction to the mechanics of elastic and plastic deformation of solids and structural components [M]. 3rd ed. Oxford: Butterworth-Heinemann, 1997.

[18] GUO Xue-yi, CHEN Yuan-lin, WANG Qin-meng, WANG Song-song, TIAN Qing-hua. Copper and arsenic substance flow analysis of pyrometallurgical process for copper production [J]. Transactions of Nonferrous Metals Society of China, 2022, 32(1): 364−376.

[19] FERESHTEH-SANIEE F, BARATI F, BADNAVA H, FALLAH-NEJAD K H. An exponential material model for prediction of the flow curves of several AZ series magnesium alloys in tension and compression [J]. Materials & Design, 2012, 35: 1−11.

[20] AYALA J S, de MOURA H L, AMARAL R D L, OLIVEIRA JUNIOR F D A, NUNHEZ J R, de CASTILHO G J. Two-dimensional shear rate field and flow structures of a pseudoplastic fluid in a stirred tank using particle image velocimetry [J]. Chemical Engineering Science, 2022, 248: 117198.

[21] WANG Hui-yuan, FENG Ting-ting, ZHANG Lei, LIU Chun-guo, PAN Yue, ZHA Min, NAN Xiao-long, WANG Cheng, JIANG Qi-chuan. Achieving a weak basal texture in a Mg−6Al−3Sn alloy by wave-shaped die rolling [J]. Materials & Design, 2015 88: 157−161.

[22] CHE Bo, LU Li-wei, WU Zhi-qiang, ZHANG Hua, MA Min, LUO Jun, ZHAO Hong-mei. Dynamic recrystallization behavior and microstructure evolution of a new Mg−6Zn−1Gd−1Er alloy with and without pre-aging treatment [J]. Materials Characterization, 2021, 181: 111506.

[23] CHANG Li-li, GUO Jing, SU Xiao-jing. Effect of Y on microstructure evolution and mechanical properties of Mg−4Li−3Al alloys [J]. Transactions of Nonferrous Metals Society of China, 2021, 31(12): 3691−3702.

[24] KIM S H, YOU B S, YIM C D, SEO Y M. Texture and microstructure changes in asymmetrically hot rolled AZ31 magnesium alloy sheets [J]. Materials Letters, 2005, 59(29/30): 3876−3880.

[25] WANG Wen-ke, ZHANG Wen-cong, CHEN Wen-zhen, CUI Guo-rong, WANG Er-de. Effect of initial texture on the bending behavior, microstructure and texture evolution of ZK60 magnesium alloy during the bending process [J]. Journal of Alloys and Compounds, 2018, 737: 505−514.

[26] CHE Bo, LU Li-wei, KANG Wei, LUO Jun, MA Min, LIU Long-fei. Hot deformation behavior and processing map of a new type Mg−6Zn−1Gd−1Er alloy [J]. Journal of Alloys and Compounds, 2021, 862: 158700.

[27] ALIZADEH R, WANG Jing-ya, LLORCA J. Precipitate strengthening of pyramidal slip in Mg−Zn alloys [J]. Materials Science and Engineering: A, 2021, 804: 140697.

[28] CHE Bo, LU Li-wei, ZHANG Jia-long, ZHANG Jing-huai, MA Min, WANG Li-fei, QI Fu-gang. Effects of cryogenic treatment on microstructure and mechanical properties of AZ31 magnesium alloy rolled at different paths [J]. Materials Science and Engineering: A, 2022, 832: 142475.

[29] JIANG Ming-guang, XU Chao, YAN Hong, FAN Guo-hua, NAKATA T, LAO Chang-shi, CHEN Rong-shi, KAMADO S, HAN En-hou, LU Bing-heng. Unveiling the formation of basal texture variations based on twinning and dynamic recrystallization in AZ31 magnesium alloy during extrusion [J]. Acta Materialia, 2018, 157: 53−71.

[30] ZHANG Jing, XI Guo-qiang, WAN Xin, FANG chao. The dislocation-twin interaction and evolution of twin boundary in AZ31 Mg alloy [J]. Acta Materialia, 2017, 133: 208−216.

[31] ZHAO Feng, SUO Tao, CHEN Bin, LI Yu-long. Strength-ductility combination of fine-grained magnesium alloy with high deformation twin density [J]. Journal of Alloys and Compounds, 2019, 798: 350−359.

[32] LENTZ M, RISSE M, SCHAEFER N, REIMERS W, BEYERLEIN I J. Strength and ductility with $\{10\bar{1}1\}-\{10\bar{1}2\}$ double twinning in a magnesium alloy [J]. Nature Communications, 2016, 7: 11068.

[33] LIU Hong-yu, WANG Yang, LI Bing-cheng, MA Xiao-chun, WU Rui-zhi, HOU Le-gan, ZHANG Jing-huai, ZHANG Mi-lin. Effect of cryogenic rolling process on microstructure and mechanical properties of Mg−14Li−1Al alloy [J]. Materials Characterization, 2019, 157: 109903.

[34] LU Song-he, WU Di, CHEN Rong-shi, HAN En-hou. Reasonable utilization of $\{10\bar{1}2\}$ twin for optimizing microstructure and improving mechanical property in a

Mg−Gd−Y alloy [J]. Materials & Design, 2020, 191: 108600.
[35] ZENG Xiao-qin, ZHU Qing-chun, LI Yang-xin, DING Wen-jiang. Second phase particle strengthening in magnesium alloys [J]. Materials China, 2019, 38(3): 109−204. (in Chinese)
[36] CALLISTER D W Jr, RETHWISCH G. David. Materials science and engineering: An introduction [M]. 9th ed. Hoboken: Wiley, 2014.
[37] ZECEVIC M, BEYERLEIN I J, KNEZEVIC M. Activity of pyramidal I and II ⟨*c*+*a*⟩ slip in Mg alloys as revealed by texture development [J]. Journal of the Mechanics and Physics of Solids, 2018, 111: 290−307.
[38] WANG Wen-ke, ZHANG Wen-cong, CHEN Wen-zhen, CUI Guo-rong, WANG Er-de. Evolution of microstructure, texture and mechanical properties of ZK60 magnesium alloy in a single rolling pass [J]. Materials Science and Engineering: A, 2018, 724: 486−492.
[39] HAN Ting-zhuang, HUANG Guang-sheng, MA Li-feng, WANG Guan-gang, WANG Li-fei, PAN Fu-sheng. Evolution of microstructure and mechanical properties of AZ31 Mg alloy sheets processed by accumulated extrusion bonding with different relative orientation [J]. Journal of Alloys and Compounds, 2019, 784: 584−591.
[40] SUN Qi, FU Xue-song, CHEN Guo-qing, DONG Hong-gang, ZHOU Wen-long. Improving the mechanical properties of a friction stir welded AZ31 joint by adjusting the microstructure and texture [J]. Journal of Materials Research and Technology, 2022, 21: 2326−2337.
[41] RUAN Yu-tao, HU Li, ZHANG Shuo-zuo, CHEN Qiang, ZHOU Tao, XIANG Liu, JIANG Shu-yong. Influence of loading direction on mechanical behavior, microstructure characteristic and texture evolution of WE43-T4 magnesium alloy undergoing uniaxial compression [J]. Materials Today Communications, 2022, 31: 103613.
[42] CUI Chao, HE Jian, WANG Wen-ke, CHEN Wen-zhen, ZHANG Wen-cong. Microstructure, texture and mechanical properties of extruded AZ31 Mg alloy during small strain multi-directional forging with gradient cooling [J]. Journal of Alloys and Compounds, 2022, 909: 164795.
[43] CALDATTO DALAN F, de LIMA ANDREANI G F, TRAVESSA D N, FAIZOV I A, FAIZOVA S, CARDOSO K R. Effect of ECAP processing on distribution of second phase particles, hardness and electrical conductivity of Cu−0.81Cr−0.07Zr alloy [J]. Transactions of Nonferrous Metals Society of China, 2022, 32(1): 217−232.
[44] LIU Xiao-huan, LI Yan-sheng, MAN Yi, WANG Jin-hui, XU Rui. Precipitation and recrystallization of HPT-processed Mg−Sm−Ca alloy at low temperatures [J]. Materials Letters, 2020, 277: 128252.
[45] TIAN Yan-zhong, LI Lin-lin, LI Jing-jing, YANG Yang, LI Song, QIN Gao-wu. Correlating strength and hardness of high-entropy alloys [J]. Advanced Engineering Materials, 2021, 23(8): 2001514.

不同模具角度下反复弯曲−压平变形工艺对 AZ31 镁合金板材显微组织演变和变形行为的影响

李旻昊[1]，卢立伟[1,2,3]，范宇田[3]，马 旻[3]，吴志强[3]，周 涛[4]，齐福刚[5]，张 华[6]

1. 湖南科技大学 机电工程学院，湘潭 411201；
2. 湖南科技大学 难加工材料高效精密加工湖南省重点实验室，湘潭 411201；
3. 湖南科技大学 材料科学与工程学院，湘潭 411201；
4. 重庆理工大学 材料科学与工程学院，重庆 400054；
5. 湘潭大学 材料科学与工程学院，湘潭 411105；
6. 烟台大学 精准材料高等研究院，烟台 264005

摘 要：采用不同角度模具的反复弯曲−压平变形工艺制备 AZ31 镁合金板材。通过 FEM、OM、EBSD 和硬度计研究 AZ31 镁合金在反复弯曲−压平变形过程中的显微组织演变和变形行为。结果表明，150°/150°模具在所有三组实验中都表现出最佳性能。随着道次的增加，合金的等效应变由于剪切和弯曲作用而显著提高。经过 4 道次后，合金的平均晶粒尺寸显著细化至 1.7 μm，基面织构被弱化，这是非基面滑移、动态再结晶和孪生引起的；尤其是锥面⟨*c*+*a*⟩滑移有利于引发动态再结晶和孪生。合金的硬度值达到 HV 77，这是滑移、孪生和动态再结晶竞争产生的显微组织和织构综合作用的结果。

关键词：AZ31 镁合金板材；显微组织演变；变形行为；反复弯曲−压平工艺；模具角度

(Edited by Wei-ping CHEN)